(Received 2 March 2024, Accepted 19 May 2024, Scheduled 28 May 2024)

Decoupling Control of Six-Pole Axial-Radial Active Magnetic Bearing Based on Improved Linear Active Disturbance Rejection Optimized by Least Square Support Vector Machine

Zhen Wang[1], Gai Liu[2,*], Jintao Ju[3], and Huangqiu Zhu[1,*]

[1]School of Electrical and Information Engineering, Jiangsu University, Zhenjiang 212013, China
[2]School of Electrical and Control Engineering, Xuzhou University of Technology, Xuzhou 221018, China
[3]School of Electrical and Information Engineering, Changzhou Institute of Technology, Changzhou 213032, China

ABSTRACT: To improve the coupling problem between radial degrees of freedom in six-pole axialradial active magnetic (AR-AMB), a decoupling control method based on an improved linear active disturbance rejection decoupling control strategy optimized by the least square support vector machine (LSSVM-ILADRC) is proposed. Firstly, the structure and working principle of the six-pole AR-AMB are introduced, and the mathematical model of suspension force is derived. Secondly, cascaded linear extended state observers (LESOs) are used to estimate the disturbance in degrees of freedom step by step, with LESO1 providing an initial estimate of the total disturbance, and LESO2 estimating and compensating for the difference between the initial estimate and the actual disturbance. The regression prediction function of LSSVM is employed to enhance the response speed and estimation accuracy of the LESO to the disturbance. Finally, the simulation and experimental research show that the proposed LSSVM-ILADRC decoupling control method has better decoupling performance and anti-interference performance than the ILADRC decoupling control method.

1. INTRODUCTION

As the core component of computer numerical control (CNC) machine tools, motorized spindle uses bearings to support the rotor. The appearance of magnetic bearings improves the friction, pollution, and other problems caused by the contact between the stator and rotor, which have many advantages, such as no contact, no lubrication, and no wear [1, 2]. At present, magnetic bearings have been widely used in turbo molecular pumps, aerospace, flywheel energy storage, and other fields [3–5]. Three-pole magnetic bearings driven by the inverter effectively solve the problems of high cost and large volume caused by the DC amplifier of four-pole and eight-pole magnetic bearings. However, to improve the nonlinear relationship between the suspension force and current of three-pole magnetic bearings, and further improve the bearing capacity and space utilization rate, six-pole axial-radial active magnetic bearing (AR-AMB) is proposed [6–8].

The quality of the control method directly affects the overall performance of the magnetic bearing system, such as sliding mode control [9], adaptive control [10], and model predictive control [11]. Six-pole AR-AMB is a nonlinear and strongly coupled system. To obtain high control accuracy and good dynamic and static performance, the study of its decoupling control is essential. In [12], a state feedback decoupling control strategy for an AMB high-speed flywheel rotor system is presented. It is easier to design various controllers and achieve both good control performance and good internal stability. In [13], an active disturbance rejection control strategy (ADRC) based on a back propagation (BP) neural network is put forward. The method has strong robustness and adaptability to the uncertainty of the magnetic bearing model and the variation of external disturbance. In [14], a dynamic decoupling control method based on neural network inverse system theory is adopted. The advantages of this method are strong robustness and high adaptability, and the results show that the whole control system has better dynamic and static performance. However, the neural network is prone to local optimization; there is a transition fit; and large-scale data sets lead to a long training time. In [15], a decoupling control strategy is proposed that combines the inverse system method with internal model control. The stability and robustness problems induced by current-mode linearization have been successfully solved. Simulated and experimental results demonstrate that the proposed strategy has high decoupling precision and strong robustness performances. However, this control method relies on the precise mathematical model of the controlled object, especially for complex systems, and the internal model control design is complex. In [16], an active disturbance rejection control (ADRC) strategy is adopted to suppress model errors effectively caused by the linearized model and has strong adaptability and robustness. The simulation results show that the system has good dynamic and static performance. Its biggest feature is that it does not rely on the precise mathematical model of the controlled object and has strong anti-interference ability.

However, traditional ADRC suffers from several drawbacks, including a significant number of parameters that are often challenging to adjust. Additionally, its disturbance tracking speed

* Corresponding authors: Gai Liu (lg_just@163.com); Huangqiu Zhu (zhuhuangqiu@ujs.edu.cn).

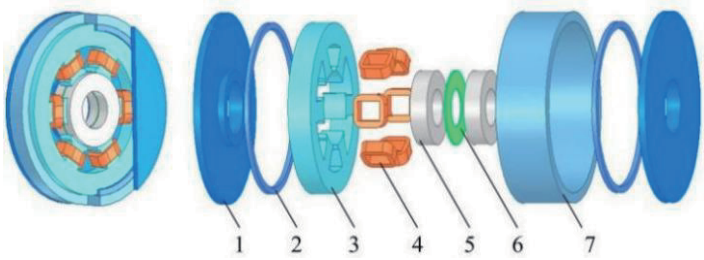

FIGURE 1. The structure of the six-pole AR-AMB (1) Axial stator. (2) Axial coils. (3) Radial stator. (4) Radial coils. (5) Rotor. (6) Magnetic insulation aluminum ring. (7) Sleeve.

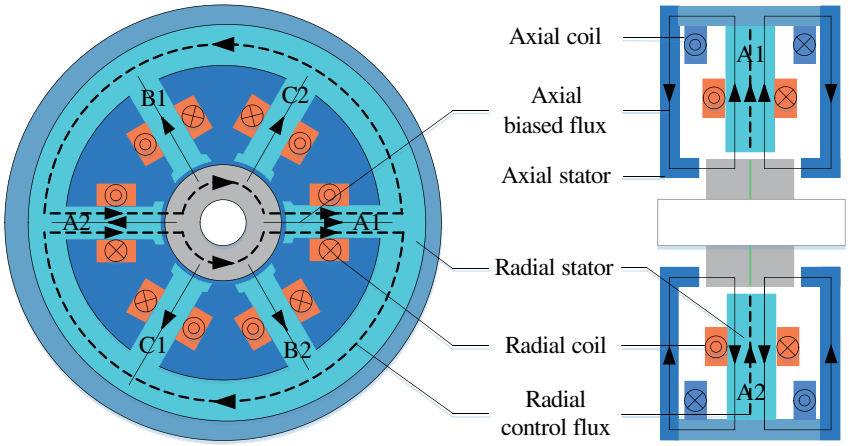

FIGURE 2. The magnetic circuit of the six-pole AR-AMB.

and accuracy are limited, posing a challenge for achieving optimal performance. Given these limitations, enhancing the traditional ADRC becomes highly necessary. In [17], a controller that integrates repetitive control with linear ADRC (LADRC) is proposed. This innovative approach aims to maintain the dynamic response of the system while effectively eliminating periodic disturbances caused by rotor vibrations. Nevertheless, the design of a repetitive controller can be intricate and computationally intensive, thus posing its own set of challenges. In [18], a LADRC/nonlinear ADRC (NLADRC) switching control scheme combining the advantages of LADRC and NLADRC is proposed, which can improve the tracking accuracy of disturbance, and the stability characteristics of the design are analyzed. However, this kind of switching control makes parameter adjustment more difficult and puts higher requirements on the extended state observer (ESO). In [19], an improved LADRC is proposed, which has good position tracking performance by designing a two-stage cascade linear ESO (LESO). However, the above improved LADRC robustness and anti-interference performance are at the expense of fast response, so the dynamic response speed of the system will be reduced. Least squares support vector machine (LSSVM) follows the principle of structural risk minimization and has high training speed and good fitting ability which is used to optimize the ADRC to bring the possibility of decoupling of the magnetic bearing system [20].

In this paper, the decoupling control of the six-pole AR-AMB is proposed through the application of the LSSVM-ILADRC. In Section 2, the working principle of the six-pole AR-AMB is thoroughly analyzed, and its mathematical model is subsequently derived. In Section 3, the key parameters of the LESO are determined based on the cascaded form of the ILADRC, and a decoupling controller optimized by the LSSVM algorithm is meticulously designed. In Sections 4 and 5, the feasibility and superiority of the proposed method are verified through simulations and experiments, with comparisons made to the decoupling control strategy based on ILADRC.

2. OPERATION PRINCIPLE AND MATHEMATICAL MODEL OF THE SIX-POLE AR-AMB

2.1. Operation Principle of the Six-Pole AR-AMB

The 3D structure of the six-pole AR-AMB is shown in Fig. 1, which is primarily composed of an axial stator, radial coils, a radial stator, axial coils, a rotor, a magnetic isolation aluminum ring, and a sleeve. The axial coils are securely affixed in the middle of the sleeves by a wire clamp and are operated by a switching power amplifier. Two radial coils, opposing each other and sharing the same winding direction, are joined in series, forming a single phase, which results in three phases for the six poles. These three phases of the six-pole configuration are connected in a star formation and are powered by a three-phase power inverter. The six magnetic poles, designated as A1, A2, B1, B2, C1, and C2, are separated from the outer wall of the rotor by an air gap measuring 0.5 mm. The magnetic circuit of the six-pole AR-AMB is illustrated in Fig. 2.

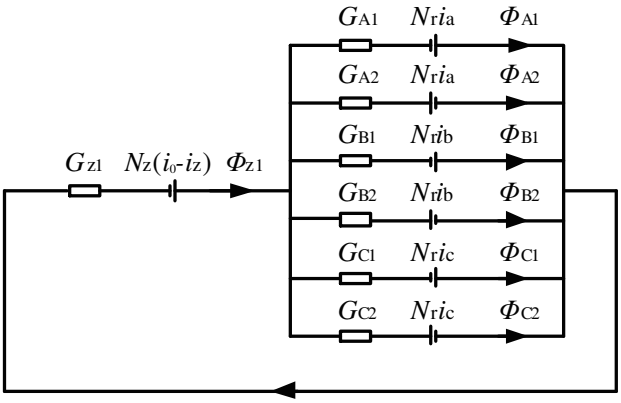

FIGURE 3. Equivalent magnetic circuit of six-pole AR-AMB.

The axial bias magnetic flux flow generated by the axial coils is the dotted line with an arrow, forming a loop among the sleeve, axial stator, axial air gap, rotor, radial air gap, and radial stator. The radial control flux magnetic flow generated by the radial coils is the solid line with an arrow, forming a loop among the radial stator, radial air gap, rotor, and radial air gap. When the rotor is in the equilibrium position, the air gap around the rotor is uniform, and only the axial bias coils are energized to generate the bias magnetic flux to overcome the gravity of the rotor. In the radial direction, if the rotor is disturbed in the A1 direction and the air gap in this direction reduced, a negative control current is applied to the A-phase coils, causing the bias magnetic flux in the A2 direction air gap to be superimposed with the control magnetic flux, and the bias magnetic flux in the A1 direction air gap is offset against the control magnetic flux, thus generating a suspension force along direction A2 to pull the rotor back to the equilibrium position.

The design requirements for the six-pole AR-AMB are a radial suspension force of 200 N and an axial suspension force of 250 N. Generally, increasing the current can increase the suspension force, but as the control current reaches a certain value, the magnetic induction intensity exceeds the saturation magnetic induction intensity. At this time, the suspension force will increase slowly, and the power consumption generated by the current will increase sharply. At the same time, the nonlinear relationship between the suspension force and the control current will be strengthened. To ensure that the ferromagnetic material operates in the linear region, a saturation magnetic induction intensity of 0.8 T is set, and the final determination of the current size is ± 1.25 A. The radial coil has 160 turns, and the axial coil has 200 turns [21].

2.2. Dynamic Equation of the Six-Pole AR-AMB

In the given scenario, when the axial coil operates alone, an equivalent magnetic circuit diagram as shown in Fig. 3 is obtained. This diagram is derived from the magnetic flux flow direction as illustrated in Fig. 1.

To solve this circuit, Kirchhoff's current and voltage law is applied. By doing so, we can determine the expressions for magnetic flux in both the axial and radial air gaps, which are as follows:

$$\begin{cases} \Phi_{z1} = \dfrac{G_r G_{z1}}{G_{z1}+G_r} N_z \left(i_0 - i_z\right), \\ \Phi_{z2} = \dfrac{G_r G_{z1}}{G_{z1}+G_r} N_z \left(i_0 + i_z\right) \\ \Phi_{A1} = \dfrac{G_{z1} G_{A1}}{G_{z1}+G_r} N_z \left(i_0 - i_z\right) \\ \qquad + \dfrac{G_{z2} G_{A1}}{G_{z2}+G_r} N_z \left(i_0 + i_z\right) + N_r i_a G_{A1} \\ \Phi_{A2} = \dfrac{G_{z1} G_{A2}}{G_{z1}+G_r} N_z \left(i_0 - i_z\right) \\ \qquad + \dfrac{G_{z2} G_{A2}}{G_{z2}+G_r} N_z \left(i_0 + i_z\right) - N_r i_a G_{A2} \\ \Phi_{B1} = \dfrac{G_{z1} G_{B1}}{G_{z1}+G_r} N_z \left(i_0 - i_z\right) \\ \qquad + \dfrac{G_{z2} G_{B1}}{G_{z2}+G_r} N_z \left(i_0 + i_z\right) + N_r i_b G_{B1} \\ \Phi_{B2} = \dfrac{G_{z1} G_{B2}}{G_{z1}+G_r} N_z \left(i_0 - i_z\right) \\ \qquad + \dfrac{G_{z2} G_{B2}}{G_{z2}+G_r} N_z \left(i_0 + i_z\right) - N_r i_b G_{B2} \\ \Phi_{C1} = \dfrac{G_{z1} G_{C1}}{G_{z1}+G_r} N_z \left(i_0 - i_z\right) \\ \qquad + \dfrac{G_{z2} G_{C1}}{G_{z2}+G_r} N_z \left(i_0 + i_z\right) + N_r i_c G_{C1} \\ \Phi_{C2} = \dfrac{G_{z1} G_{C2}}{G_{z1}+G_r} N_z \left(i_0 - i_z\right) \\ \qquad + \dfrac{G_{z2} G_{C2}}{G_{z2}+G_r} N_z \left(i_0 + i_z\right) - N_r i_c G_{C2} \end{cases} \tag{1}$$

where $G_r = G_{A1} + G_{A2} + G_{B1} + G_{B2} + G_{C1} + G_{C2}$. N_z is the number of turns in the axial coils, and i_0 and i_z are the

bias current and control current in the axial coils. z_1 and z_2 are right and left axial air gap magnetic fluxes. G_{z1} and G_{z2} are the corresponding permeabilities. N_r is the number of turns in the radial coils. i_j ($j = a, b, c$) are the three-phase control current. Φ_{k1}, Φ_{k2} ($k = A, B, C$) are the magnetic fluxes of the radial air gap. G_{k1} and G_{k2} ($k = A, B, C$) are the corresponding permeabilities.

According to Newton's second law, the dynamics equation of the six-pole AR-AMB rotor is:

$$\begin{cases} m\ddot{x} = F_x - f_x \\ m\ddot{y} = F_y - f_y \\ m\ddot{z} = F_z - f_z \\ J_x\ddot{\theta}_x = -l_a(F_y - f_y) - J_z\Omega\dot{\theta}_y \\ J_y\ddot{\theta}_y = l_a(F_x - f_x) + J_z\Omega\dot{\theta}_x \end{cases} \tag{2}$$

where m represents the rotor mass. f_x, f_y, and f_z denote the external disturbance forces acting in the x, y, and z directions, respectively. J_x, J_y, and J_z are the moments of inertia generated by the rotor around the respective axes. Notably, J_x and J_y are equal to J_d. Ω represents the mechanical angular velocity of the rotor rotating about the z-axis. θ_x and θ_y indicate the rotation angles of the rotor around the x and y axes, respectively. l_a and l_b signify the length of the six-pole AR-AMB and the distance from the center of mass O to the auxiliary bearing.

From the relation between the variables, the dynamic equation is rewritten as:

$$\begin{cases} \ddot{x} = \dfrac{k_r}{m}\left(1 + \dfrac{ml_a^2}{J_d}\right)x - \dfrac{J_z\Omega l_a}{J_d(l_a + l_b)}\dot{y} \\ \qquad + \dfrac{k_{ir}}{m}\left(1 + \dfrac{ml_a^2}{J_d}\right)i_x - \left(\dfrac{1}{m} + \dfrac{l_a^2}{J_y}\right)f_x \\ \ddot{y} = \dfrac{k_r}{m}\left(1 + \dfrac{ml_a^2}{J_d}\right)y + \dfrac{J_z\Omega l_a}{J_d(l_a + l_b)}\dot{x} \\ \qquad - \dfrac{k_{ir}}{m}\left(1 + \dfrac{ml_a^2}{J_d}\right)i_y - \left(\dfrac{1}{m} + \dfrac{l_a^2}{J_x}\right)f_y \\ \ddot{z} = \dfrac{k_z}{m}z + \dfrac{k_{iz}}{m}i_z - \dfrac{1}{m}f_z \end{cases} \tag{3}$$

3. DECOUPLING CONTROLLER OF THE SIX-POLE AR-AMB

3.1. LSSVM Algorithm

The principle of LSSVM regression is to use the nonlinear mapping function $\varphi(x)$ to map the nonlinear regression of low-dimensional input vectors to the linear identification of high-dimensional eigenvectors. For a training sample with an n-dimensional input vector $\mathbf{x} = [x_1, x_2, \ldots, x_n]^T$ and corresponding output vector $\mathbf{y} = [y_1, y_2, \ldots, y_n]^T$, the nonlinear function expression is $y(x) = \mathbf{w}^T\varphi(x) + b$, where $\mathbf{w}$ is the weight of the input vector, and b is the deviation quantity.

Based on the principle of structural risk minimization, the optimization problem is defined as:

$$\begin{cases} \min J(w, e) = \dfrac{1}{2}w^T w + \dfrac{1}{2}\gamma\sum_{i=1}^{n} e_i^2 \\ s.t.\ \ y_i = w^T\varphi(x_i) + b + e_i,\ \ i = 1, 2, \ldots, n \end{cases} \tag{4}$$

where γ is the regularization parameter, and e is the difference between the training result y_i and the actual output y.

The Lagrange function is obtained:

$$L(w, b, e, \alpha) = \min J(w, e) - \sum_{i=1}^{n} a_i\left(w^T\varphi(x_i) + b + e_i - y_i\right) \tag{5}$$

where α_i is a Lagrange multiplier.

The analytical solution of the optimization problem is obtained by the Karush-Kuhn-Tucker (KKT) optimal condition.

$$\begin{bmatrix} 0 & I_n^T \\ I_n & \mathbf{\Omega} + \frac{1}{\gamma}I_n \end{bmatrix}\begin{bmatrix} b \\ a \end{bmatrix} = \begin{bmatrix} 0 \\ y \end{bmatrix} \tag{6}$$

where $\mathbf{I}_n$ is the identity matrix; $\mathbf{\Omega}$ is a diagonal matrix of nth order; the diagonal elements are Gaussian kernel functions $K(x_i, x)$, $K(x_i, x) = \exp(-||x_i x)||/2\sigma^2$; σ^2 is the width of kernel functions.

The LSSVM regression prediction equation is as follows:

$$y(x) = \sum_{i=1}^{n} a_i K(x_i, x) + b \tag{7}$$

3.2. ILADRC Algorithm

The structure of ILADRC is mainly composed of linear state error feedback (LSEF) and two cascaded LESOs. LESO1 preliminarily estimates the total disturbance to obtain the disturbance v_3 of the system, which takes it as the known part and feeds it back to LESO2 in real time. LESO2 comprehensively estimates the disturbance to obtain the total disturbance z_3 of the system, and the two cascaded LESOS jointly undertake the estimation of the disturbance, which can effectively improve the estimation accuracy of the disturbance.

Using linear weighted sum instead of nonlinear feedback, the LSEF expression established in ILADRC is:

$$\begin{cases} u_0 = k_p(v - z_1) - k_d z_2 \\ u = u_0 - \dfrac{z_3}{b_0} \end{cases} \tag{8}$$

where k_p and k_d are controller gains. $k_p = 8$, $k_d = 0.004$.

The established LESO1 expression is:

$$\begin{cases} \dot{v}_1 = v_2 - h_{01}e_1 \\ \dot{v}_2 = v_3 - h_{02}e_3 + b_0 u \\ \dot{v}_3 = -h_{03}e_1 \\ e_1 = v_1 - y \end{cases} \tag{9}$$

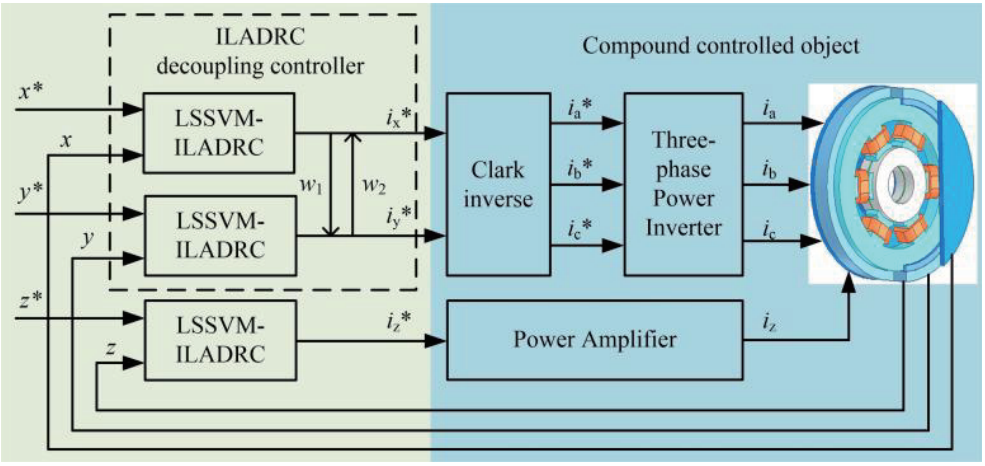

FIGURE 4. The block diagram of decoupling control of the six-pole AR-AMB.

where v_1 is the observed value of output y; v_2 is the differential of v_1; e_1 is the observation error; b_0 is the compensation factor; u is the control quantity; h_{01}, h_{02}, and h_{03} are the gains of LESO1; ω_0 is the observer bandwidth, $\omega = 495$.

The established LESO2 expression is:

$$\begin{cases} \dot{z}_1 = z_2 - \beta_{01} e_2 \\ \dot{z}_2 = z_3 + v_3 - \beta_{02} e_2 + b_0 u \\ \dot{z}_3 = -\beta_{03} e_2 \\ e_2 = z_1 - y \end{cases} \tag{10}$$

where β_{01}, β_{02}, and β_{03} are the gains of LESO2, $\beta_{01} \approx h_{01} = 3\omega$, $\beta_{02} \approx h_{02} = 3\omega^2$, $\beta_{03} \approx h_{03} = \omega^3$.

According to the derived mathematical model of magnetic bearings, the approximate expression of b is $b = k_c k_i k_s / m$; k_c is the amplifier gain coefficient, $k_c = 0.1$ A/V. k_i is the force-current stiffness coefficient, $k_i = 189.43$ N/A. k_s is the sensor gain coefficient, $k_s = 8000$ V/m, $m = 2.8$ kg. Therefore, the calculation gives $b = 54122.86$.

3.3. Decoupling Controller Based on LSSVM-ILADRC

The coupling between the radial degrees of freedom is seen as an external disturbance of the system. The actual external disturbance of the rotor in the axial and radial degrees of freedom is considered an internal disturbance of the system. The simplified equation of state expression substitutes the total disturbance on each degree of freedom.

$$\begin{cases} \ddot{x} = k_{11} i_x + k_{13} x + w_x \\ \ddot{y} = k_{21} i_y + k_{23} y + w_y \\ \ddot{z} = k_{31} z + k_{32} i_z + w_z \end{cases} \tag{11}$$

where k_{11}, k_{13}, k_{21}, k_{23}, k_{31}, and k_{32} are the coefficients in front of the corresponding terms, respectively. ω_x, ω_y, and ω_z represent the total disturbance on each degree of freedom, respectively.

The six-pole AR-AMB system can be divided into three independent uncoupled second-order linear subsystems. Each of these subsystems is controlled by a single LSSVM-ILADRC. The three LSSVM-ILADRCs use the same structure and algorithm. By utilizing the LESO in ILADRC to estimate and compensate for the total disturbance on each degree of freedom, the six-pole AR-AMB can be transformed from a strongly coupled, nonlinear system to an uncoupled, linear system. The corresponding block diagram of decoupling control is shown in Fig. 4.

The block diagram of decoupling control based on LSSVM-ILADRC in the x direction is shown in Fig. 5. Let's take the displacement control in the x direction as an example. To apply LSSVM to ILADRC, we collect samples by taking the observed value z_{1x} and its differential z_{2x} of LESO2 to the actual displacement of the rotor as input vectors and the predicted value f of the disturbance as the corresponding output vector. We then use the LSSVM model of Matlab to train the input sample **z** and output sample **f**. This helps us obtain the LSSVM regression prediction model about the disturbance, which can be obtained according to Equations (4)–(7).

The LSSVM regression prediction model predicts the disturbance value f according to the observation value z_{1x} and its differential z_{2x}. f is added to the real-time observation value $z_{3x+}v_{3x}$ of the external disturbance of the LESO model and compensated by $1/b_{0x}$ to obtain control quantity u_x. In addition to being used as the input of the object, u_x is also compensated by b_{0x} and added to the predicted disturbance value f, which is used as the input of the LESO model again to complete real-time observation and adjustment of the disturbance. Optimizing ILADRC by utilizing the characteristics of fast training speed and more convenient determination of model parameters of the LSSVM regression prediction model can effectively reduce the burden of LESO on disturbance observation and improve observation accuracy. The corresponding optimization process is shown in Fig. 6.

In the above LSSVM algorithm, the regularization parameter γ and bandwidth σ^2 of the kernel function need to be set to achieve an accurate regression model. Due to the existence of auxiliary bearings, the movement range of the rotor is ± 0.25 mm, so the sinusoidal signal with a frequency of

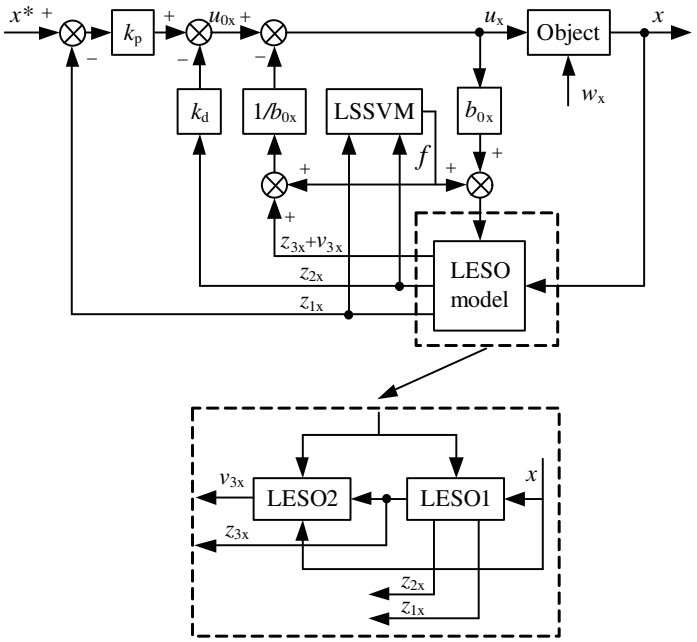

FIGURE 5. The block diagram of decoupling control based on LSSVM-ILADRC in the x direction.

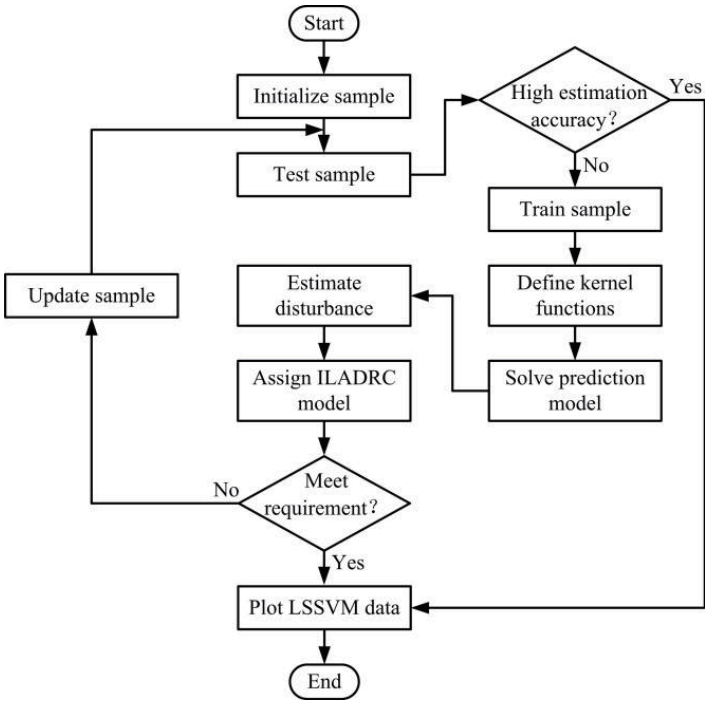

FIGURE 6. The flowchart of disturbance prediction based on LSSVM-ILADRC.

100 Hz and an amplitude of 0.25 mm is used as the excitation, and the whole data acquisition process is carried out under the PID closed-loop control system. In the sample collection process of applying LSSVM to ILADRC, the observed value z_1 and its differential z_2 of LESO2 to the actual displacement of the rotor are taken as input vectors, and the predicted value f of the disturbance is taken as the corresponding output vector.

80% of the collected sample data is used as training samples to generate the LSSVM learning machine, and the remaining 20% is used as test samples to verify the regression prediction model. Root mean square error (RMSE) is used as the performance index of the model evaluation, and its expression is as follows:

$$F = \left\{ \frac{1}{M} \sum_{i=1}^{M} \left[y_{reg}\left(i\right) - y_{test}\left(i\right) \right]^2 \right\}^{-1} \tag{12}$$

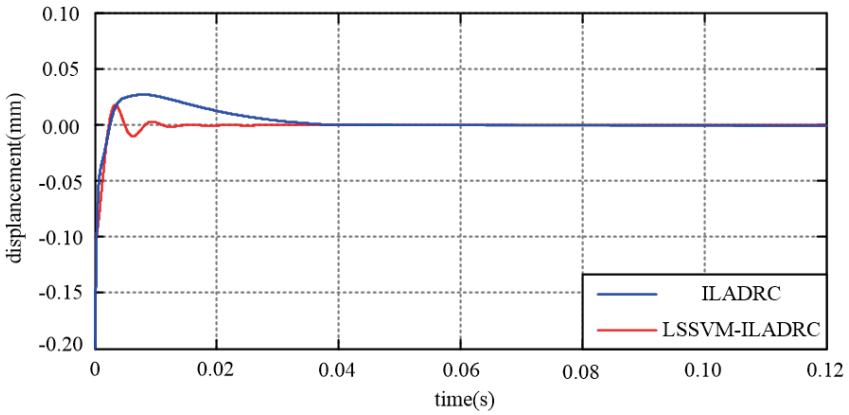

FIGURE 7. The response curves when the rotor suspend in the x direction.

where M is the total number of the samples in the test set; $y_{reg}(i)$ is the regression output of the i-th input $x_{test}(i)$ in the training sample; $y_{test}(i)$ is the i-th output of the test sample.

The sampling time is 1 s; the sampling accuracy is 1 ms; and a total of 1000 input and output vectors are obtained. In order to prevent ill-conditioned data in the calculation process and improve the accuracy of the model, all samples are normalized:

$$\text{norm}\,(X) = \frac{X - \text{mean}\,(X)}{\text{std}\,(X)} \tag{13}$$

where norm(**X**) is the normalization result, and mean(**X**) and std(**X**) are the mean and standard deviation of the input samples, respectively.

4. SIMULATION TEST

The ILADRC optimized through LSSVM algorithms is thoroughly analyzed using MATLAB. The regularization parameter γ is optimized within the range of [0, 1000] while the bandwidth σ^2 of the kernel function is optimized within the range of [0, 1].

4.1. Response Simulation

Due to the presence of auxiliary bearings, the remaining air gap length is 0.25 mm, so the initial displacement of -0.2 mm is set in the x direction, and no initial displacement is set in the y direction. The response curves when the rotor suspends in the x direction are shown in Fig. 7. Compared with the LADRC decoupling control strategy, the rotor needs 0.062 s to achieve stable suspension, and the rotor only needs 0.028 s to achieve stable suspension based on the LSSVM-ILADRC decoupling control strategy. Simulation results show that the proposed method has a small overshoot and higher control accuracy.

4.2. Suspension Force Simulation

The relationship between the suspension force and the displacement is shown in Fig. 8. It can be seen that the force-displacement stiffness coefficient in the x direction is 810.55 N/mm. When the incoming current is constant, there

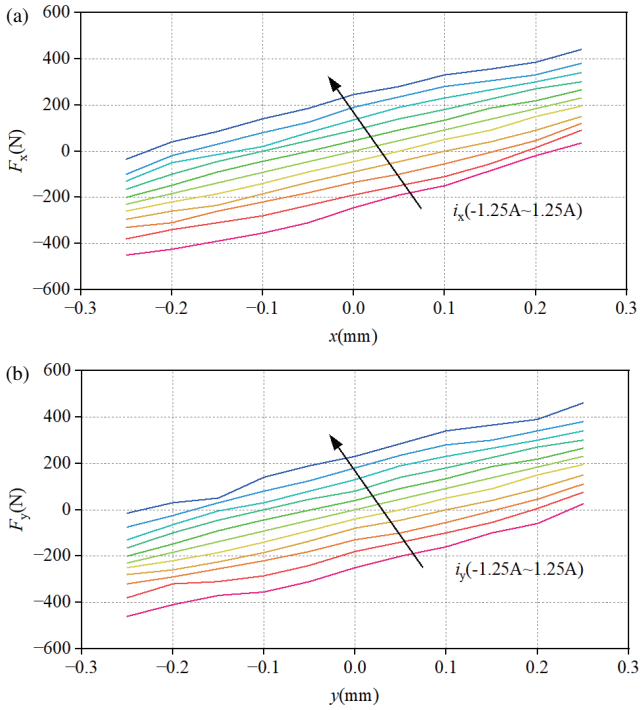

FIGURE 8. The relationship between suspension force and displacement. (a) x direction. (b) y direction.

is a good linear relationship between force and displacement near the equilibrium position. As the rotor gradually moves away from the equilibrium position, the linear relationship between force and displacement becomes worse. When the rotor reaches the maximum deviation of ± 0.25 mm, it is considered that the relationship between force and displacement is nonlinear. Therefore, the relationship between force and displacement is considered linear only when the rotor rotates near the equilibrium position.

4.3. Anti-Interference Simulation

At 0.02 s, 30 N external disturbance force is applied in the x direction, and after 0.05 s, 15 N external disturbance force is applied again in the x direction. The response curves in the ra-

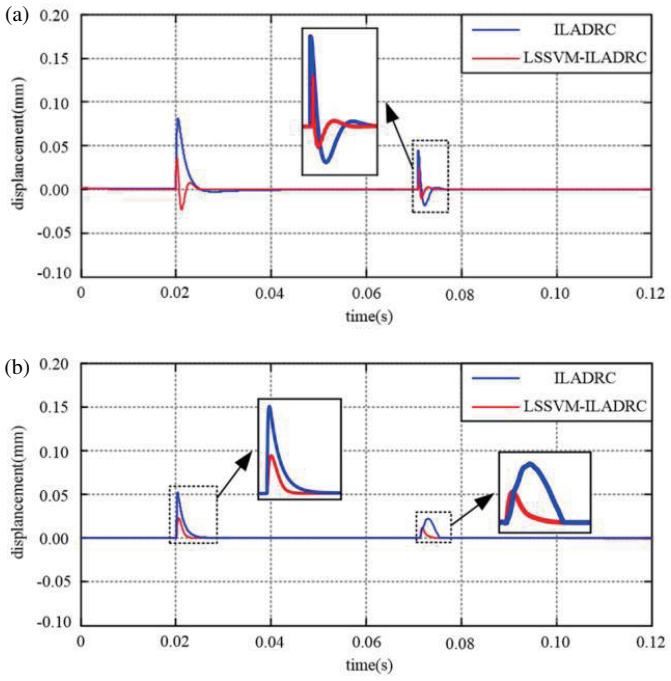

FIGURE 9. The response curves when the disturbance is applied on the rotor in the x direction. (a) x direction. (b) y direction.

dial direction when the disturbance is applied in the x direction are shown in Fig. 9. In the case of the LADRC decoupling control strategy, the rotor returns to the equilibrium position after 0.025 s adjustment time in the x direction, with the maximum offset being 0.1 mm. At the same time, the rotor also has a 0.065 mm deviation in the y direction, with an adjustment time of 0.008 s. Based on the LSSVM-ILADRC decoupling control strategy, the rotor can return to the equilibrium position after only 0.005 s adjustment time with an offset being only 0.03 mm, and an offset in the y direction is less than half of the LADRC decoupling control strategy. The simulation results show that the proposed method has a stronger anti-interference ability and can realize the decoupling of the magnetic bearing system more effectively, reducing the influence of disturbance on the system position.

4.4. Estimation Simulation

Initially, a sinusoidal interference force of $50\sin(4\pi t)$ is imposed on the system, persisting for 3/2 cycles. Subsequently, a force of $10\cos(4\pi t - \pi/2)$ is introduced. The estimated disturbance curves are shown in Fig. 10. The LADRC decoupling control strategy commences tracking the disturbance after 0.15 seconds. Notably, as the amplitude of the disturbance varies, the tracking error increases. Conversely, the LSSVM-ILADRC decoupling control strategy commences tracking within merely 0.07 seconds. This strategy effectively maintains continuous tracking even when the disturbance amplitude changes. Simulation results indicate that the proposed method exhibits superior response speed and tracking accuracy, particularly evident in the reduced estimation error during disturbance variations.

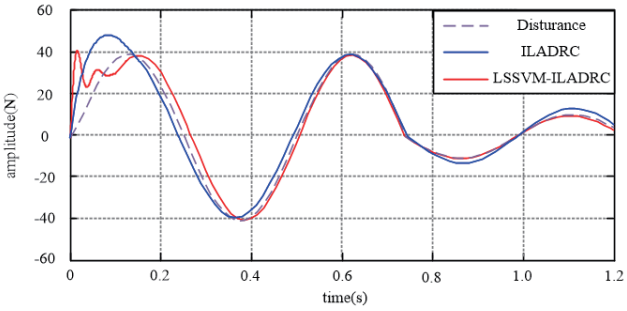

FIGURE 10. The estimation curves of the disturbance.

5. EXPERIMENT RESEARCH

In order to verify the effectiveness of the decoupling control strategy of the six-pole AR-AMB based on the proposed method, the experimental platform is constructed, and the control system is shown in Fig. 11, which includes the six-pole AR-AMB, digital signal processor (DSP) board, radial power circuit board, etc. The floating experiment, anti-interference, and decoupling experiment are performed. The main parameters of the six-pole AR-AMB are given in Table 1.

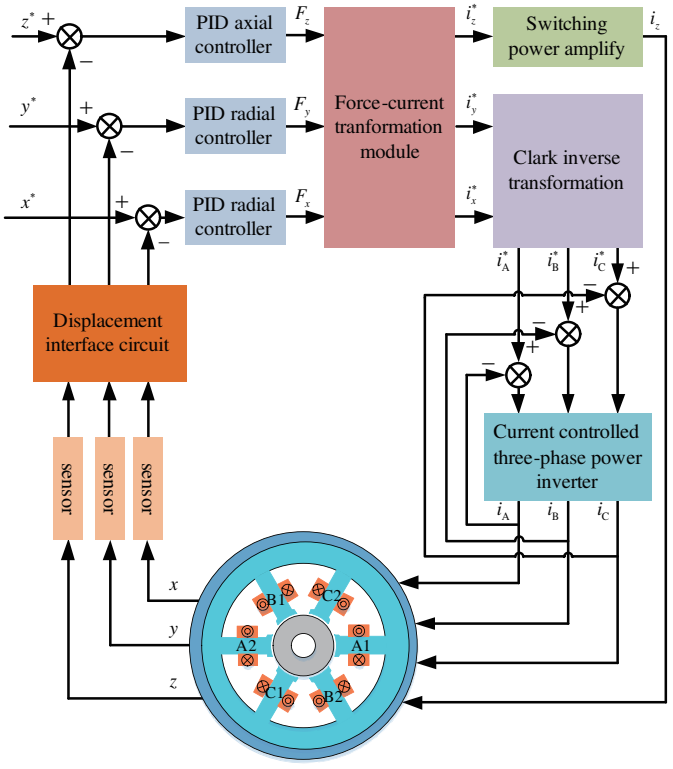

FIGURE 11. The control system of the six-pole AR-AMB.

The core of the six-pole AR-AMB digital control system is the TMS320F28335 DSP chip designed by TI company. Taking the reset circuit as an example, the diagram of the chip's reset circuit is shown in Fig. 12. The initial level of the nXRS end is low. During the power-on reset process, capacitor C_{r3} is in a constant charging state, and the charging time depends on the product of resistor R_{r3} and capacitor C_{r3}. If the power on reset time is insufficient, the system program may fall into a

TABLE 1. The main parameters of the six-pole AR-AMB.

Parameters	Value
Pole arc angle β	$2\pi/9$
Air gap length δ_0	0.5 mm
Thickness of pole shoe d_1	4 mm
Axial length of magnetic pole l_1	25 mm
Radial width length of magnetic pole d_2	16 mm
Inner radius of stator yoke r_3	50 mm
Outer radius of stator yoke r_4	68 mm
Axial length of rotor l_2	40 mm

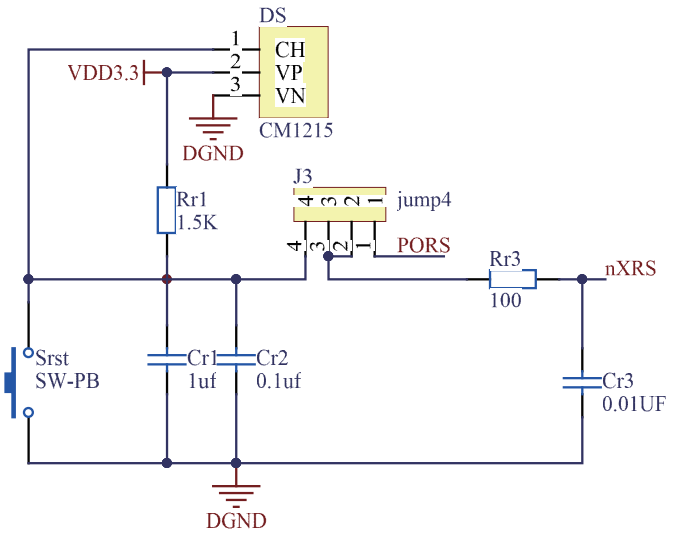

FIGURE 12. The diagram of the reset circuit.

chaotic state, leading to the inability to execute smoothly after burning. Therefore, to ensure the stability of the reset process, it is usually necessary to increase the capacitance of capacitor C_{r3} to reduce program abnormalities caused by insufficient reset. After the power-on reset is completed, the port level will be completely converted from low to high [22].

The function of the power drive board is to enhance the driving ability of the pulse width modulation (PWM) signal generated by the control board, thereby driving the frequency conversion module and generating a three-phase control current. Taking the current sampling circuit as an example, the schematic diagram of the current sampling circuit is shown in Fig. 13. The sensor uses the CSNE151 Hall current sensor introduced by Honeywell company, which has no electrical connection between the primary and secondary sides, ensuring the electrical safety of the secondary side IC. Its input is positive and negative 12 A, and the output is positive and negative 24 mA, corresponding to a 100 Ω sampling resistance, which outputs a positive and negative 2.4 V voltage signal. The first stage operational amplifier amplifies it in reverse by 0.625 times, and the second stage operational amplifier raises it by 1.5 V, outputting a voltage signal of 0–3 V to meet the requirements of the DSP analog-to-digital conversion module [23].

5.1. Speed Variation Experiment

When the speed accelerates from 1500 r/min to 3000 r/min, the speed and displacement waveforms in the x and y directions are shown in Fig. 14. The ILADRC decoupling control strategy is adopted as shown in Fig. 14(a). The disturbance amplitudes are 40 µm and 35 µm in the x- and y-directions, respectively, and the adjustment time is 193 ms. The LSSVM-ILADRC decoupling control strategy is adopted as shown in Fig. 14(b). The disturbance amplitudes are 31 µm and 30 µm in the x- and y-directionsa, respectively, and the adjustment time is 176 ms. When the rotational speed rises, the displacement change amplitude in x- and y-directions based on the LSSVM-ILADRC decoupling control strategy is smaller than that of the ILADRC decoupling control strategy. The above analysis verifies that the proposed method has better dynamic performance and can enter stable suspension faster at different rotational speeds.

5.2. Floating Experiment

When the coils are not powered, the magnetic bearing rotor comes to a stop on the auxiliary bearing due to gravity. However, when the coils are energized, the floating waveforms of the rotor are shown in Fig. 15. The ILADRC decoupling control strategy is illustrated in Fig. 15(a). When the coils are energized, the rotor achieves stable suspension after 44 ms, 49 ms, and 37 ms in the x-, y-, and z-directions, respectively, due to the electromagnetic force generated by the energized coils. On the other hand, the LSSVM-ILADRC decoupling control strategy, as shown in Fig. 15(b), allows the rotor to achieve stable suspension after 40 ms, 44 ms, and 25 ms in the x-, y- and z-directions, respectively. The above analysis confirms that the proposed method has a shorter response time and better floating performance.

5.3. Anti-Interference Experiment

The motion state of the rotor under external disturbance force is shown in Fig. 16. The ILADRC decoupling control strategy is shown in Fig. 16(a). When the rotor is affected by a 30 N external disturbance force in the radial direction and leaves the equilibrium position, the displacement of the rotor in the x and y directions is 44 µm and 21 µm, and the recovery time of returning to the equilibrium position is 35 ms and 3 ms, respectively. The LSSVM-ILADRC decoupling control strategy is adopted as shown in Fig. 16(b). The displacement of the rotor in the x and y directions is 27 µm and 15 µm, and the recovery time for returning to the equilibrium position is 24 ms and 20 ms, respectively. The two methods have almost no displacement fluctuation in the z direction. It shows that there is no coupling between axial and radial degrees of freedom, which is consistent with the theoretical analysis. The above analysis verifies that the proposed method has better anti-interference performance.

5.4. Decoupling Experiment

The decoupling experimental waveforms in the radial directions when a 40 N disturbance is applied on the rotor in the x direction are shown in Fig. 17. The ILADRC decoupling control

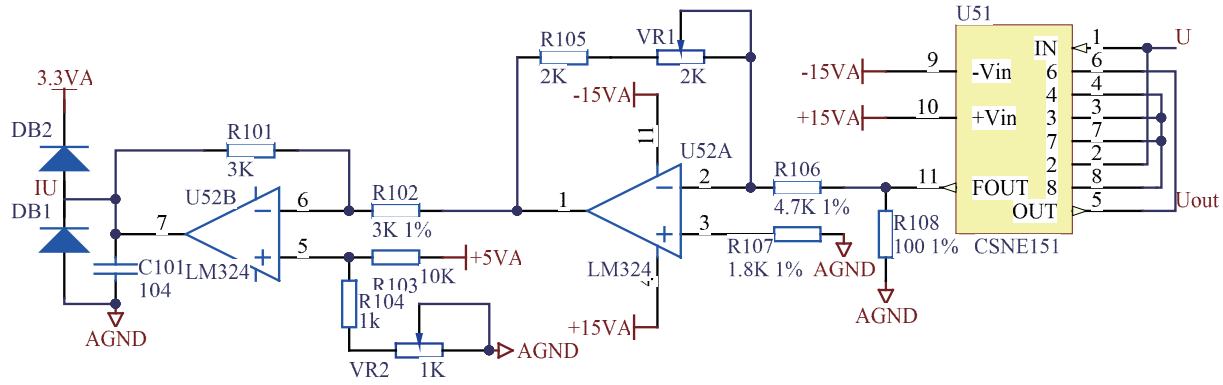

FIGURE 13. The diagram of the current sampling circuit.

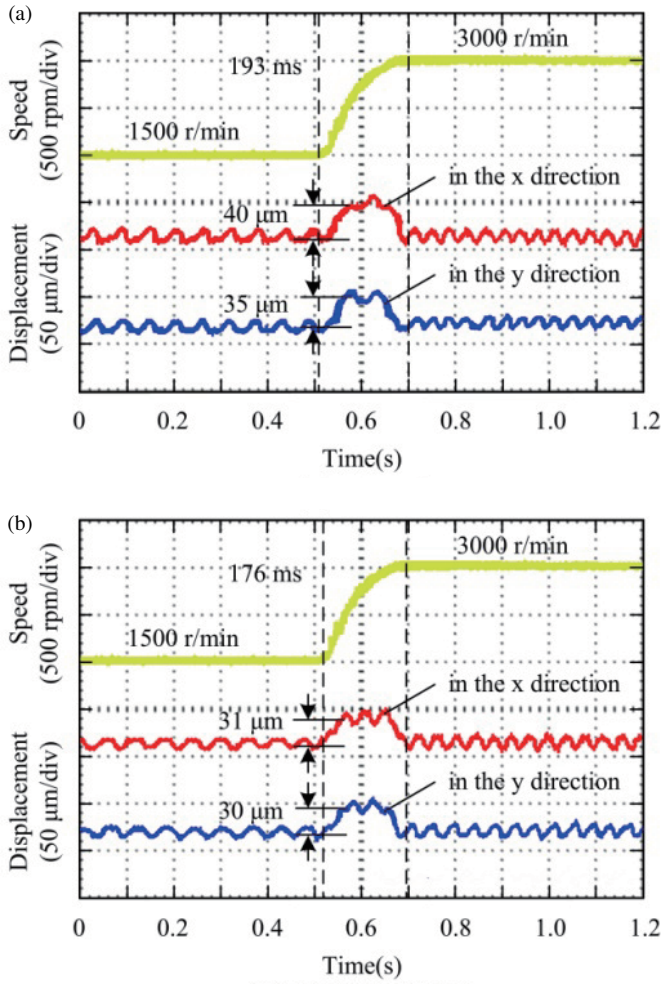

FIGURE 14. The experimental waveforms of rotational speed and radial displacement in the x- and y-direction. (a) ILADRC. (b) LSSVM-IIADRC.

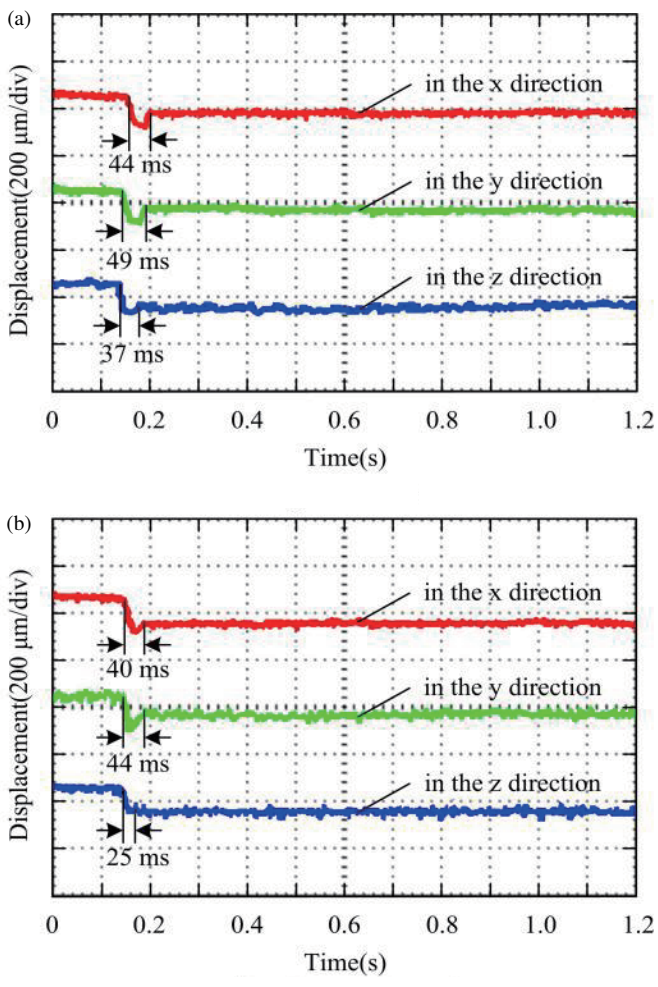

FIGURE 15. The floating waveforms of the six-pole AR-AMB. (a) ILADRC. (b) LSSVM-IIADRC.

strategy is presented in Fig. 17(a), where the rotor takes 21 ms to return to the equilibrium position in the x direction and shifts in the y direction. On the other hand, the LSSVM-ILADRC decoupling control strategy shown in Fig. 17(b) is adopted, where the rotor only needs 6 ms to return to the equilibrium position, reducing the adjustment time by 15 ms, and the overthrow is smaller. Moreover, there is almost no displacement in the y direction. The above analysis confirms that the proposed method can achieve better decoupling control between the radial degrees of freedom.

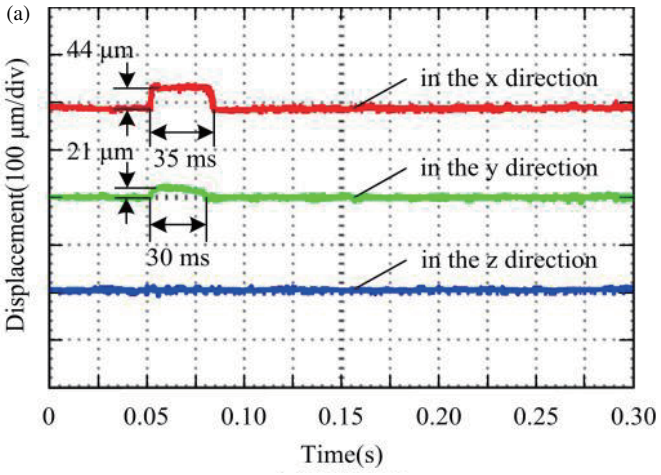

FIGURE 16. The anti-interference waveforms of the six-pole AR-AMB. (a) ILADRC. (b) LSSVM-IIADRC.

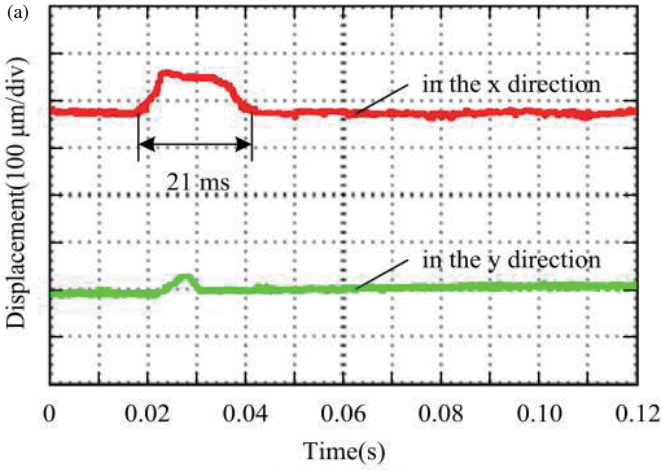

FIGURE 17. The decoupling waveforms of the six-pole AR-AMB when the disturbance is applied on the rotor in the x direction. (a) ILADRC. (b) LSSVM-IIADRC.

6. CONCLUSION

Based on the characteristics of multivariable, nonlinear, and strong coupling of the six-pole AR-AMB, the decoupling control strategy based on the ILADRC optimized by the LSSVM is proposed. The effectiveness of the proposed decoupling control strategy is verified by simulation and experiment. The obtained conclusions are as follows:

1. In the ILADRC controller, b is the only parameter related to the magnetic bearing system, and its determination greatly reduces the difficulty of controller design. The cascaded LESO can effectively reduce the observation burden of disturbance and improve the observation accuracy.

2. The regression prediction model in LSSVM is used to optimize the LESO. Based on the characteristics of a fast rate of convergence, the speed of response to disturbance is improved, and the observation accuracy is further improved. The ILADRC optimized by LSSVM realizes the decoupling between the radial degrees of freedom of the six-pole AR-AMB, which has good anti-interference performance.

3. Future work will focus on improving decoupling performance while reducing the complexity of the controller of the six-pole AR-AMB.

ACKNOWLEDGEMENT

This project was sponsored in part by National Natural Science Foundational of China (62273168,62303075).

REFERENCES

[1] Chen, S.-L., S.-Y. Lin, and C.-S. Toh, "Adaptive unbalance compensation for a three-pole active magnetic bearing system," *IEEE Transactions on Industrial Electronics*, Vol. 67, No. 3, 2097–2106, 2020.

[2] Jiang, D., T. Li, Z. Hu, and H. Sun, "Novel topologies of power electronics converter as active magnetic bearing drive," *IEEE Transactions on Industrial Electronics*, Vol. 67, No. 2, 950–959, 2020.

[3] Jin, Z., X. Sun, L. Chen, and Z. Yang, "Robust multi-objective optimization of a 3-pole active magnetic bearing based on combined curves with climbing algorithm," *IEEE Transactions on Industrial Electronics*, Vol. 69, No. 6, 5491–5501, 2022.

[4] Noh, M. D., S.-R. Cho, J.-H. Kyung, S.-K. Ro, and J.-K. Park, "Design and implementation of a fault-tolerant magnetic bearing system for turbo-molecular vacuum pump," *IEEE/ASME Transactions on Mechatronics*, Vol. 10, No. 6, 626–631, 2005.

[5] Li, X., A. Palazzolo, and Z. Wang, "A combination 5-DOF active magnetic bearing for energy storage flywheels," *IEEE Transactions on Transportation Electrification*, Vol. 7, No. 4, 2344–2355, 2021.

[6] Cole, M. O. T. and W. Fakkaew, "An active magnetic bearing for thin-walled rotors: Vibrational dynamics and stabilizing control," *IEEE/ASME Transactions on Mechatronics*, Vol. 23, No. 6, 2859–2869, 2018.

[7] Wang, H., Z. Wu, K. Liu, J. Wei, and H. Hu, "Modeling and control strategies of a novel axial hybrid magnetic bearing for flywheel energy storage system," *IEEE/ASME Transactions on Mechatronics*, Vol. 27, No. 5, 3819–3829, 2022.

[8] Xie, Y., D. Jiang, F. Hu, and Z. Liu, "Research on common mode EMI and its reduction for active magnetic bearings," *IEEE Transactions on Power Electronics*, Vol. 38, No. 4, 4246–4250, 2023.

[9] Zad, H. S., T. I. Khan, and I. Lazoglu, "Design and adaptive sliding-mode control of hybrid magnetic bearings," *IEEE Transactions on Industrial Electronics*, Vol. 65, No. 3, 2537–2547, 2018.

[10] Chen, Z., Z. Lin, and Y. Li, "Output feedback control of an active magnetic bearing system based on adaptive command filtered backstepping," in *2019 Chinese Control Conference (CCC)*, 3060–3065, Guangzhou, China, 2019.

[11] Morsi, A., S. M. Ahmed, A. M. Mohamed, and H. S. Abbas, "Model predictive control for an active magnetic bearing system," in *2020 IEEE 7th International Conference on Industrial Engineering and Applications (ICIEA)*, 715–720, Bangkok, Thailand, 2020.

[12] Li, Y. and C. Zhu, "Novel decoupling control and eigenstructure assignment strategies for rigid active magnetic bearing rotor system," in *2021 IEEE 4th Student Conference on Electric Machines and Systems (SCEMS)*, 1–8, Huzhou, China, 2021.

[13] Wang, S., H. Zhu, M. Wu, and W. Zhang, "Active disturbance rejection decoupling control for three-degree-of-freedom six-pole active magnetic bearing based on BP neural network," *IEEE Transactions on Applied Superconductivity*, Vol. 30, No. 4, 1–5, 2020.

[14] Hong, Y., H. Zhu, Q. Wu, J. Chen, and D. Zhu, "Dynamic decoupling control of AC-DC hybrid magnetic bearing based on neural network inverse method," in *2008 International Conference on Electrical Machines and Systems*, 3940–3944, Wuhan, China, 2008.

[15] Fang, J. and Y. Ren, "Decoupling control of magnetically suspended rotor system in control moment gyros based on an inverse system method," *IEEE/ASME Transactions on Mechatronics*, Vol. 17, No. 6, 1133–1144, 2012.

[16] Ruan, Y., Z. Yang, and H. Zhu, "Decoupling control of AC hybrid magnetic bearing based on active disturbance rejection," in *2011 International Conference on Consumer Electronics, Communications and Networks (CECNet)*, 2086–2089, Xianning, China, 2011.

[17] Wang, D. and H. Sun, "Design of repetitive controller based on linear auto disturbance rejection control for active magnetic bearing spindles," in *2017 2nd International Conference on Cybernetics, Robotics and Control (CRC)*, 106–110, Chengdu, China, 2017.

[18] Li, J., Y. Xia, X. Qi, and Z. Gao, "On the necessity, scheme, and basis of the linear–nonlinear switching in active disturbance rejection control," *IEEE Transactions on Industrial Electronics*, Vol. 64, No. 2, 1425–1435, 2017.

[19] Yang, J., X. Yang, T. Gao, and e. al., "Improved linear active disturbance rejection control method for electromagnetic levitation system," *Electric Machines & Control*, Vol. 23, No. 5, 102–109, 2019.

[20] Zhu, H. and T. Liu, "Rotor displacement self-sensing modeling of six-pole radial hybrid magnetic bearing using improved particle swarm optimization support vector machine," *IEEE Transactions on Power Electronics*, Vol. 35, No. 11, 12 296–12 306, 2020.

[21] Valagiannopoulos, C. A., "Arbitrary currents on circular cylinder with inhomogeneous cladding and RCS optimization," *Journal of Electromagnetic Waves and Applications*, Vol. 21, No. 5, 665–680, 2007.

[22] Rezal, M., D. Ishak, and M. Sabri, "High voltage magnetic pulse generation using capacitor discharge technique," *Alexandria Engineering Journal*, Vol. 53, No. 4, 803–808, 2014.

[23] Valagiannopoulos, C., "On examining the influence of a thin dielectric strip posed across the diameter of a penetrable radiating cylinder," *Progress In Electromagnetics Research C*, Vol. 3, 203–214, 2008.